Materials Science and Engineering B 271 (2021) 115298

Contents lists available at ScienceDirect

Materials Science & Engineering B

journal homepage: www.elsevier.com/locate/mseb

Probing the electrochemical properties of $NiMn_2O_4$ nanoparticles as prominent electrode materials for supercapacitor applications

Suprimkumar D. Dhas [a], Parvejha S. Maldar [a,e], Meenal D. Patil [a], Maqsood R. Waikar [b,f], Rajendra G. Sonkawade [b], Shiv K. Chakarvarti [c], Surendra K. Shinde [d], Dae Y. Kim [d], Annasaheb V. Moholkar [a,*]

[a] Thin Film Nanomaterials Laboratory, Department of Physics, Shivaji University, Kolhapur 416 004, India
[b] Radiation and Materials Research Laboratory, Department of Physics, Shivaji University, Kolhapur 416 004, India
[c] Manav Rachna International Institute of Research and Studies (MRIIRS), Faridabad and Ex-National Institute of Technology, Kurukshetra 136 119, India
[d] Department of Biological and Environmental Science, College of Life Science and Biotechnology, Dongguk University, 32 Dongguk-ro, Biomedical Campus, Ilsandong-gu, Siksa-dong, 10326 Goyang-si, Gyeonggi-do, South Korea
[e] D.Y.Patil College of Engineering, Salokhenagar, Kolhapur Maharashtra, 4163007, India
[f] Padmabhooshan Vasantraodada Patil Institute of Technology (PVPIT), Sangli (Budhgaon), Maharashtra 416304, India

ARTICLE INFO

Keywords:
Cubic spinel structure
Mixed transition metal oxides
$NiMn_2O_4$ (Nickel Manganese Oxide)
Sol–gel method
Specific capacitance
Supercapacitors

ABSTRACT

$NiMn_2O_4$ (NMO) powders have been prepared by facile sol–gel route, and the effect of annealing temperature and the concentration of KOH electrolyte on its electrochemical performance has been investigated. The electrochemical performance of the NMO electrodes is tested via a three electrode arrangement in KOH electrolyte. The NMO electrode (NMO1) prepared from the powder synthesized at a temperature of 500 °C with an approximate crystallite size of 10 nm exhibits maximum specific capacitance of 571 Fg^{-1} at a scan rate of 5 mVs^{-1} in 1 M KOH electrolyte. The specific capacitance of the NMO1 electrode is found to be improved from 571 Fg^{-1} in 1 M KOH to 762 Fg^{-1} in 6 M KOH electrolyte. The improvement in the specific capacitance of the NMO1 working electrode in 6 M KOH electrolyte can be attributed to good electrochemical utilization and an effective charge storage mechanism.

1. Introduction

Supercapacitors (SCs) have attracted much attention because of the fast rechargeability, higher power density over the batteries, and more energy storage ability as compared to conventional capacitors. The SCs have enormous energy storage capacity besides possessing the combined property of both conventional capacitor and battery [1]. Based on the charge-storage mechanism, electrochemical SCs can be classified into three categories: viz, pseudocapacitors, electrical double-layer capacitors (EDLCs), and hybrid capacitors. The conducting polymers and various metal oxides are utilized as the active electrode materials in pseudocapacitors, whereas in EDLCs carbon-based materials such as activated carbon, graphene, and carbon nanotubes are used as active electrodes. One more type of SCs is a mixture of both pseudocapacitors and EDLCs, known as a hybrid capacitor. To construct these types of SCs, the active electrode materials are made by combining either two or three distinct elements which give very large specific capacitance and enhanced energy density than pseudocapacitors or EDLCs [2]. However, all the above-mentioned SCs still suffer from some significant disadvantages such as poor cyclic life span of conductive polymers, the low capacitance of carbon-based materials and high cost of typical transition metal oxides like RuO_2 [3]. RuO_2 has been extensively investigated as a promising material due to its high specific capacitance and excellent cycling stability, but rareness and the high cost of ruthenium element are putting significant barriers to its commercialization [4]. To overcome these significant disadvantages, it is necessary to explore other alternative materials for the fabrication of supercapacitors.

Mixed transition metal oxides (MTMOs) are preferred to fabricate electrode materials for supercapacitor application over the single transition metal oxide component due to its enhanced chemical stability and electrochemical properties [5]. Out of the different MTMOs, considerable attention has been centered towards the synthesis of cubic spinel $NiMn_2O_4$ (NMO) as it offers high conductivity, outstanding electrochemical capacitance, high redox-active sites, and exceptional chemical

* Corresponding author.
E-mail address: avmoholkar@gmail.com (A.V. Moholkar).

https://doi.org/10.1016/j.mseb.2021.115298
Received 20 October 2020; Received in revised form 14 May 2021; Accepted 30 May 2021
Available online 17 June 2021

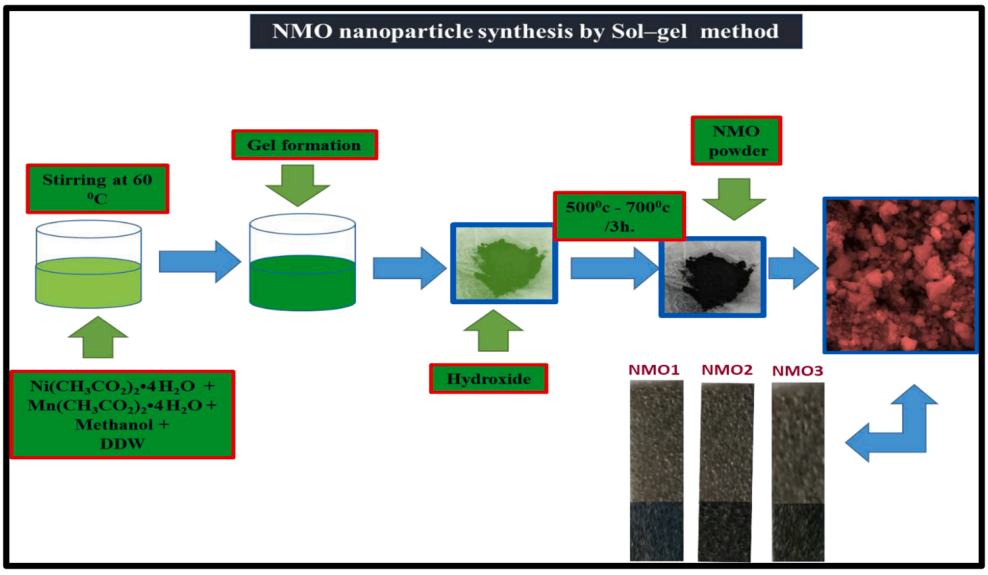

Fig. 1A. Schematic diagram of synthesis of NMO powders by sol–gel method.

stability for energetic applications. NMO has been utilized in diverse fields such as catalysis [6], supercapacitors [7], sensors [8], and negative temperature coefficient thermistors [9].The NMO nanostructures have been synthesized by various routes including, hydrothermal [3], solid-state reaction [9], sol–gel [10,11], thermal decomposition [11], spray pyrolysis [12], reflux [13], polymerization [14], and co-precipitation [15]. Among the different synthesis methods available for producing nanostructures, the non-vacuum-based sol–gel method is the cost-effective approach to prepare metal oxide nanoparticles with uniform microstructure and compositional homogeneity [16]. The sol–gel method has been used to prepare different metal oxides such as $CoMn_2O_4$, $NiCo_2O_4$, $NiFe_2O_4$, and NMO [17–19,16]. A. Ray et al. [20] reported the synthesis of porous NMO nanoparticles by sol–gel approach and showed that enhanced conductivity of the NMO nanoparticles was beneficial in improving the electrochemical performance of the NMO based supercapacitor.

In the present research work, the synthesis of porous NMO powders by a simple and inexpensive sol–gel method has been reported. The NMO electrodes are fabricated from the powders obtained at different calcination temperatures such as 500 °C, 600 °C, and 700 °C. Electrochemical performance of the NMO electrodes has been evaluated in KOH electrolyte at different concentrations such as 1 M, 2 M, 4 M, and 6 M.

2. Experimental details

2.1. Synthesis of NMO powders by sol–gel method

The chemicals nickel (II) acetate tetrahydrate (Ni $(CH_3COO)_2{\cdot}4H_2O$), 98%), manganese (II) acetate tetrahydrate (Mn $(CH_3COO)_2{\cdot}4H_2O$), 99.5%) and methanol of analytical reagent (AR) grade were used without further purification and purchased from Loba Chemie Pvt. Ltd., Mumbai (India).

NMO powders were prepared by sol–gel route. The nickel (II) acetate tetrahydrate and manganese (II) acetate tetrahydrate were used as the starting materials, whereas a mixture of methanol and double-distilled water (DDW) was used as a solvent. Stoichiometric amounts of nickel acetate and manganese acetate were dissolved separately in a mixture of methanol and DDW. Manganese acetate solution was added into the nickel acetate solution and stirred through magnetic stirring to obtain a clear homogeneous solution. The molar ratio of metal cations Mn: Ni was maintained at 2: 1 in the solution. With the addition of ammonia solution, the pH value of the mixed acetate solution was adjusted to 8. To get a sol the mixed acetate solution was stirred on a preheated hot plate at 40 °C. The dry gel was obtained by stirring the sol for 180 min at 85 °C. The gel was dried at 60 °C and ground to synthesize the powders, which were further used to carry out the calcination process. The obtained powders were calcined at different temperatures such as 500 °C, 600 °C, and 700 °C for 4 h in the air. After calcination, the powders were cooled to room temperature. Thus obtained black NMO powders were then used for various characterizations. The schematic diagram of the synthesis of NMO powder by the sol–gel route is shown in Fig. 1A. The NMO powders obtained at various calcination temperatures such as 500 °C, 600 °C, and 700 °C are labeled as NMO1, NMO2, and NMO3, respectively. The possible chemical reactions for formation of NMO through the sol–gel method are described by the following steps (I) and (II).

Step I

$$(CH_3COO)_2Ni + 2(CH_3COO)_2Mn \xrightarrow{6\,CH_3OH} Ni(OH)_2 + 2\,Mn(OH)_2 + 6\,CH_3COOCH_3$$

Nickel Acetate + Manganese Acetate → Nickel Hydroxide + Manganese Hydroxide + Methyl Acetate

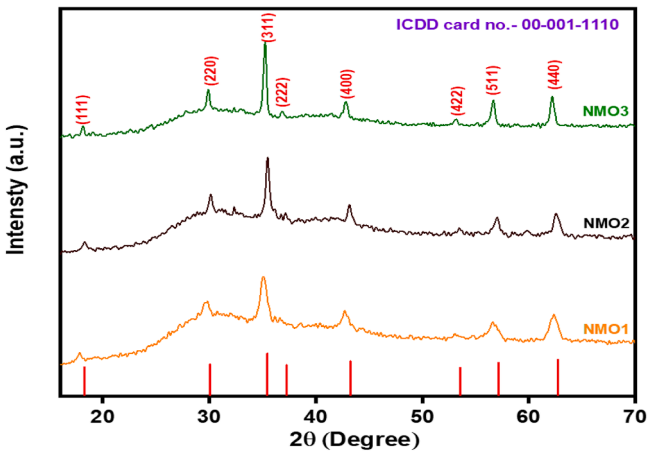

Fig. 1B. XRD patterns of the NMO1, NMO2, and NMO3 powders synthesized at calcination temperatures of 500 °C, 600 °C, and 700 °C, respectively.

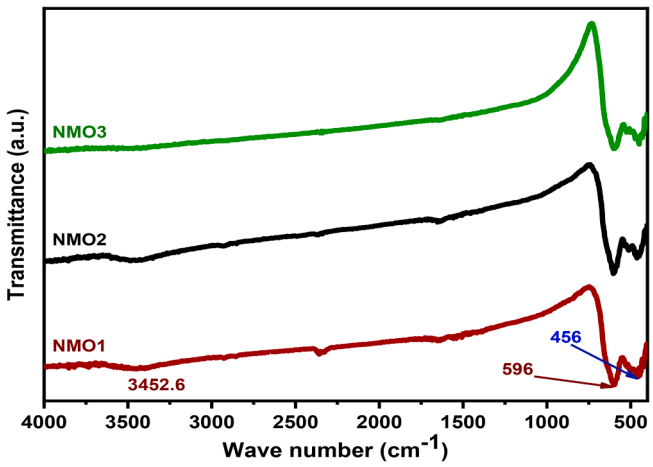

Fig. 1C. FT-IR spectra of the NMO1, NMO2, and NMO3 powder.

Step II

$$Ni(OH)_2 + 2\,Mn(OH)_2 + 6\,CH_3COOCH_3 \xrightarrow{\text{calcination}} NiMn_2O_4 + 7\,CO_2 + 11\,CH_2 + 10\,H_2$$

Nickel Manganese Oxide

2.2. Characterizations

The X-ray diffraction (XRD) of the black powders obtained at different calcination temperatures was carried out using the Bruker AXS (Diffractometer D2, Germany) with Cu (K_α) radiation over the 2θ values varying from 15° to 75°. The oxidation states of constituent elements of NMO1 powder have been evaluated by X-ray photoelectron spectroscopy (XPS), (Model-ULVAC-PHI Quantera SXM, Japan). The morphology of the powders was analyzed by field emission scanning electron microscopy (FE-SEM) (Model-JSM-6160, Japan). The Fourier-transform infrared spectroscopy (FT-IR) analysis of the powders was performed using an Alpha II spectrometer (Bruker, USA). Brunauer-Emmett-Teller (BET) (Model-NOVA1000e Quantachrome, Japan) analysis of the NMO1 powder was carried out to evaluate its surface area and pore size distribution by using nitrogen adsorption–desorption isotherms. Electrochemical properties of the NMO electrodes viz, cyclic voltammetry (CV), galvanostatic charge–discharge (GCD), and electrochemical impedance spectroscopy (EIS) were studied through potentiostat VMP3 (BioLogic, France).

2.3. Preparation of working electrode and electrochemical study

Before preparation of the NMO-Ni foam electrode, Ni-foam (3 × 1 cm^2) with a thickness of 1.6 mm was used as a current collector. The Ni-foam was cleaned with detergent, ethanol, acetone, concentrated hydrochloric acid, and DDW to eliminate the impurities and surface oxidant contents. Before examining supercapacitor properties, working electrodes were prepared by a mixture of activated NMO powders, carbon black, and polyvinylidene fluoride binder in a mass ratio of 8: 1: 1 in N-methyl-2-pyrrolidinone solvent. The mixture was sonicated to get homogeneous slurry. This slurry was drop cast onto 1 × 1 cm^2 Ni-foam and dried at 120 °C for 5 h. The electrodes prepared thus from the NMO1, NMO2, and NMO3 powders were used for electrochemical characterizations.

Electrochemical testing of the NMO electrodes for electrochemical

Table 1
Crystal structure parameters of the NMO1, NMO2, and NMO3 powders prepared by the sol–gel method.

Miller indices (*hkl*)	Interplanar distance [d_{khl}] (Å)			Lattice parameters [a = b = c] (Å)			FWHM (θ)°			Average crystallite size (nm)		
	NMO1	NMO2	NMO3	NMO1	NMO2	NMO3	NMO1	NMO2	NMO3	NMO1	NMO2	NMO3
(111)	4.97	4.84	4.89	8.61	8.39	8.47	0.49	0.52	0.31	9.7	14.9	19
(220)	3.0	2.96	2.98	8.50	8.38	8.45	0.80	0.41	0.32			
(311)	2.56	2.52	2.54	8.47	8.38	8.44	0.74	0.38	0.38			
(222)	2.42	2.41	2.41	8.37	8.37	8.37	0.88	0.55	0.40			
(400)	2.11	2.09	2.11	8.46	8.37	8.44	0.66	0.52	0.50			
(422)	1.72	1.71	1.72	8.43	8.38	8.44	1.18	0.51	0.40			
(511)	1.55	1.54	1.54	8.05	8.01	8.05	0.95	0.70	0.45			
(440)	1.48	1.48	1.49	8.42	8.38	8.43	0.89	0.57	0.44			

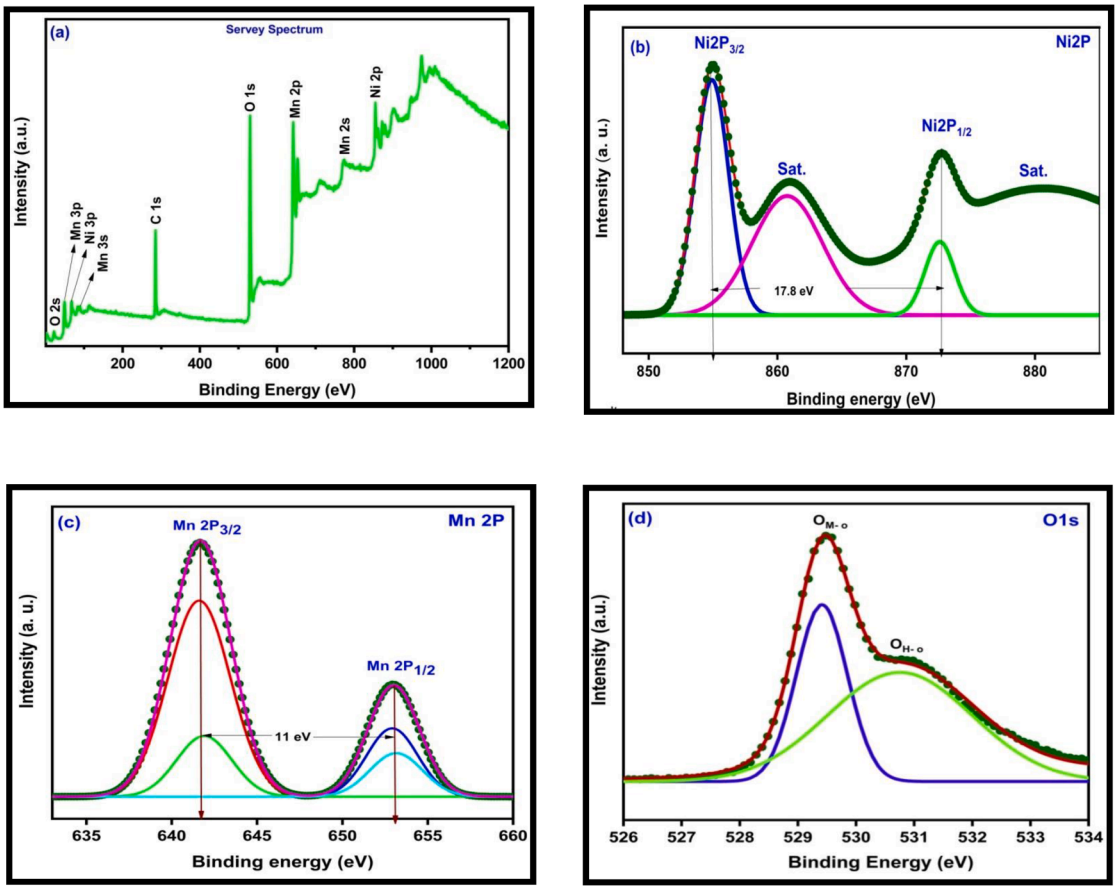

Fig. 2. (a) XPS survey scan spectrum of the NMO1 powder. XPS narrow scan spectrum of (b) Ni 2p (c) Mn 2p (d) O 1s.

capacitor was done in the standard three-electrode arrangement with the saturated calomel electrode (SCE) as a reference electrode. The NMO-Ni-foam was used as a working electrode, platinum as a counter electrode, and KOH as an electrolyte. The electrochemical properties of the NMO electrodes were investigated with CV at a scan rate of 5 mVs^{-1} to 100 mVs^{-1}, over the potential window of 0 to 0.8 V. GCD was carried out at various current densities over the potential range of 0 to 0.4 V. For the EIS measurement, an AC voltage of 5 mV was applied over the frequency range of 0.01 Hz to 100 kHz.

3. Results and discussion

3.1. XRD and FT-IR study

The crystal structure of the NMO powders synthesized by sol–gel method is examined through XRD. Fig. 1B shows the XRD patterns of NMO powders obtained at various calcination temperatures such as 500 °C, 600 °C, and 700 °C. The weak reflections observed at 2θ values of 18.29°, 29.89°, 42.82°, and 53.16° correspond to (111), (220), (400), and (420) planes, whereas strong reflections observed at 35.22°, 56.69° and 62.35° correspond to (311), (511), and (440) planes, respectively. The obtained XRD patterns of NMO powders are well-matched with a cubic structure of NMO (JCPDS card no. 00-001-1110) with the Fd-3m space group [11].

The lattice parameters a, b, and c and interplanar distance (d_{khl}) are calculated using Eqs. (1) and (2), respectively.

$$a = d_{hkl}\sqrt{h^2 + k^2 + l^2} \quad (1)$$

$$d_{hkl} = \frac{n\lambda}{2sin(\theta)} \quad (2)$$

where d_{khl} is interplanar distance, (*hkl*) are the miller indices, λ is the wavelength of X-ray used and *θ*is the Bragg's angle of reflection.

The reflections become intense with an increase in calcination temperature and improvement in the crystallinity of the NMO powders is observed. The average crystallite size (D) is calculated by Eq. (3) [21,22] and is found to be 9.7 nm, 14.9 nm, and 19 nm for the NMO1, NMO2, and NMO3, respectively.

$$D = \frac{0.9\lambda}{\beta\cos(\theta)} \quad (3)$$

where D is the crystallite size, 0.9 is the dimensionless shape factor of crystallites, λ is the wavelength of X-ray used and β is the full width at half maximum (FWHM) in radian, and *θ* is the Bragg's angle of reflection in radian. Crystal structure parameters of the NMO1, NMO2, and NMO3 powders are listed in Table 1.

FT-IR analysis is conducted to confirm the phase purity and to assess the nature of chemical bonds present in the NMO powders. The FT-IR spectra of NMO powders are shown in Fig. 1C. A broad peak is detected at 3453 cm^{-1} which can be attributed to O–H vibration and signifies that absorbed moisture exists at the surface of the NMO powders. The intense band observed at 596 cm^{-1} can be ascribed to vibration of the Ni-O atoms in the tetrahedral group, whereas the band at 456 cm^{-1} can be attributed to vibration mode of Ni-Mn-O atoms [16]. FT-IR analysis revealed the presence of spinel mixed oxide in the synthesized powders.

3.2. XPS study

The oxidation state of the constituent elements present in the NMO1 powder is evaluated by the XPS. Fig. 2 (a) represents the survey spectrum of the NMO1 powder which shows different peaks corresponding

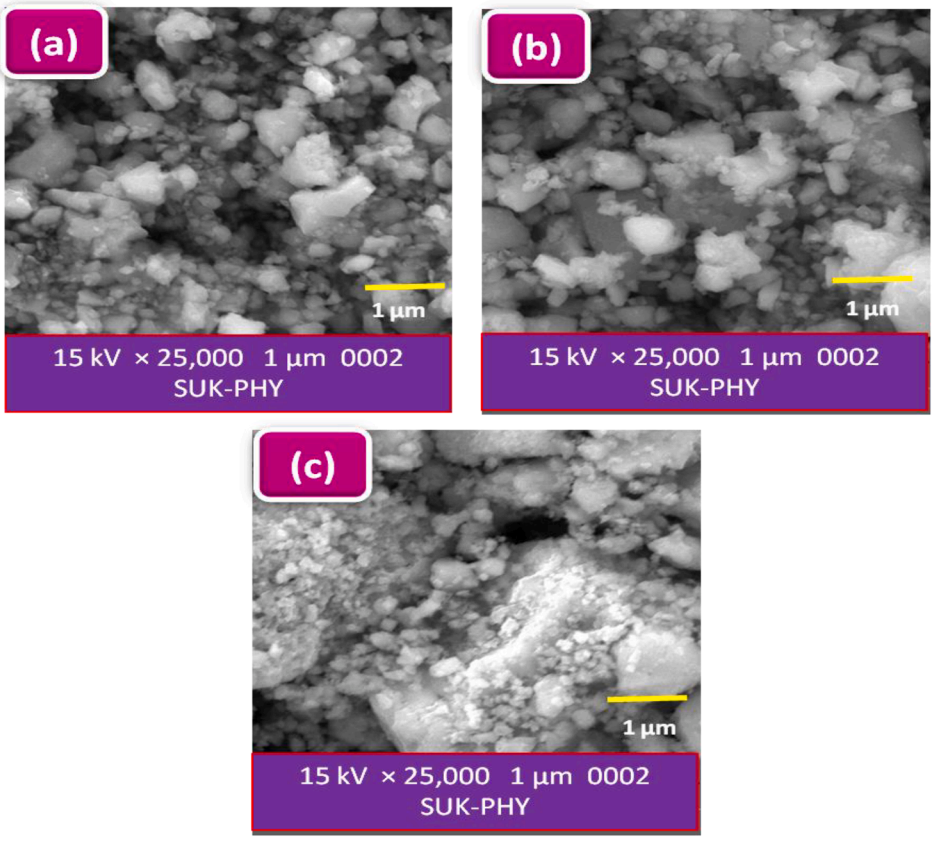

Fig. 3A. FE-SEM micrographs of the NMO powders at the magnification of ×25,000 (a) NMO1 (b) NMO2 (c) NMO3.

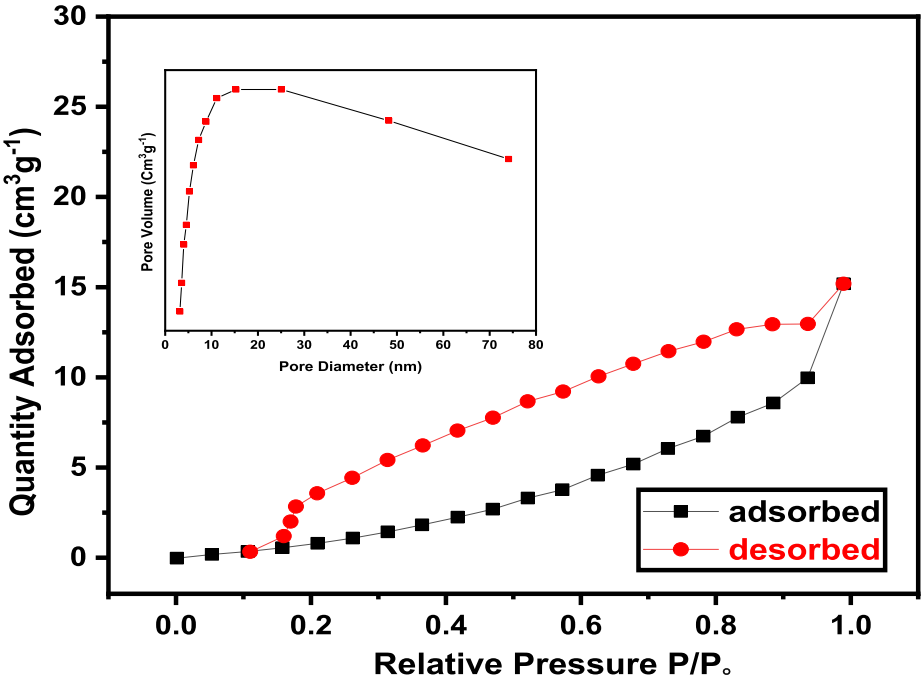

Fig. 3B. Nitrogen adsorption–desorption isotherms of the NMO1 powder. (Inset of Fig. Barrett-Joyner-Halenda (BJH) pore size distribution curve Of NMO1).

to Ni, Mn, O, and C elements. Considering the XPS peaks that are obtained on account of the different electronic transitions for Ni, Mn, and O are indexed in Fig. 2 (a). The presence of the C element is ascribed to adventitious carbon contamination due to exposure of the NMO1 powder to the atmosphere [23,24]. To allocate Ni and Mn between octahedral and tetrahedral positions in the spinel structure and to find out the oxidation state of Ni and Mn, peaks of Ni 2p and Mn 2p are further examined carefully.

For Ni, the deconvoluted two doublet peaks (spin–orbit) are assigned to Ni $2p_{1/2}$ and Ni $2p_{3/2}$ at 872 eV and 854 eV, respectively, and two

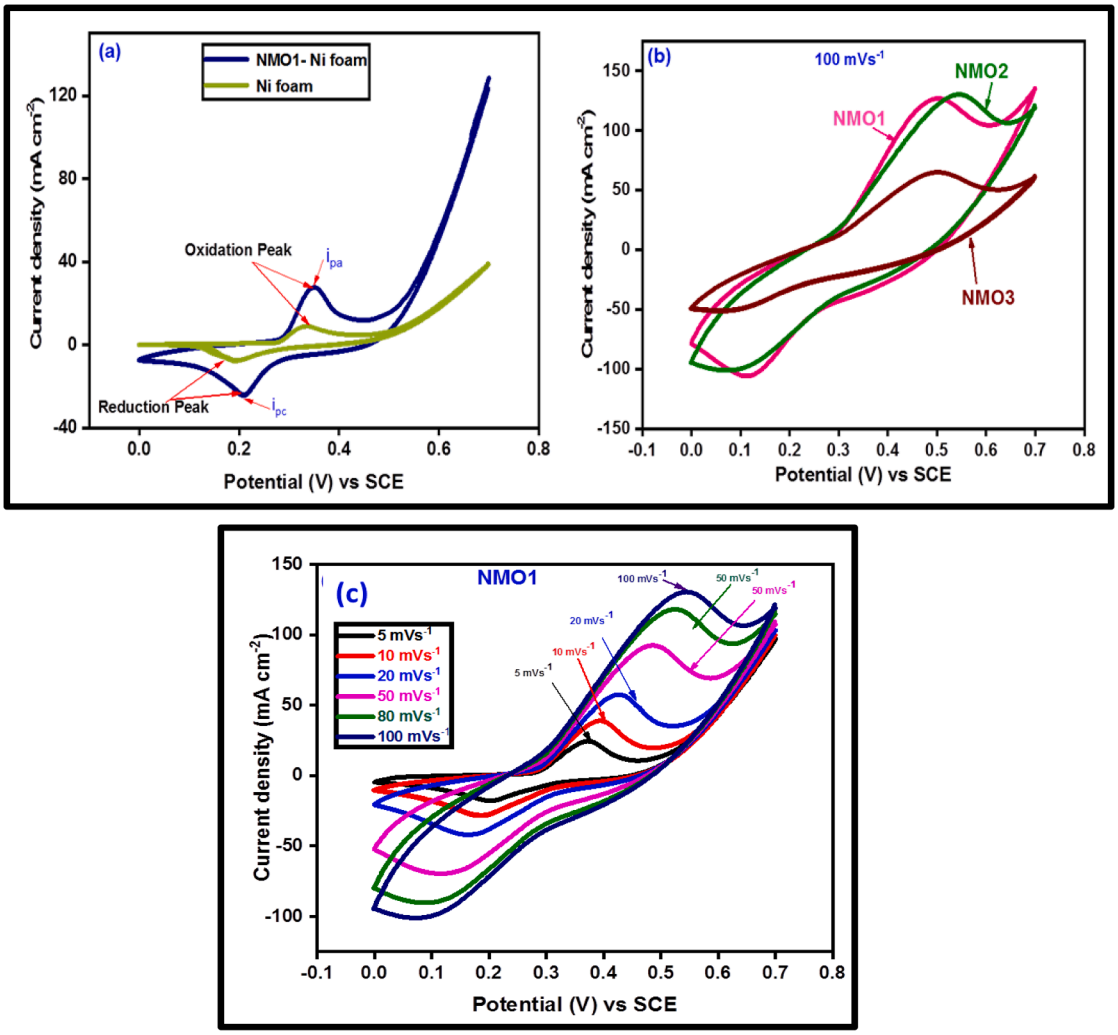

Fig. 4A. (a) Comparative CV plots of the bare Ni-foam and NMO1-Ni-foam electrode (b) Comparative CV plots of the NMO1, NMO2, and NMO3 electrodes at a scan rate of 100 mVs^{-1} in 1 M KOH electrolyte (c) CV plots of NMO1 electrode in 1 M KOH electrolyte obtained by varying scan rates.

satellite humps at 861 eV and 879 eV are displayed in Fig. 2 (b), which represents that Ni exists in divalent (spin–orbit) state [25]. Fig. 2 (c) shows a deconvoluted narrow scan spectrum of Mn, where two humps of Mn $2p_{1/2}$ and Mn $2p_{3/2}$ are found at 653.3 eV and 641.6 eV, respectively signifying the trivalent oxidation state of Mn [26]. Fig. 2 (d) shows a deconvoluted narrow scan spectrum of oxygen in which the intense hump denoted by $O_{M\text{-}O}$ at 529.6 eV is due to M−O−M bond (M denotes Ni or Mn ion) [27], and less intense hump denoted by $O_{H\text{-}O}$ at 531 eV is

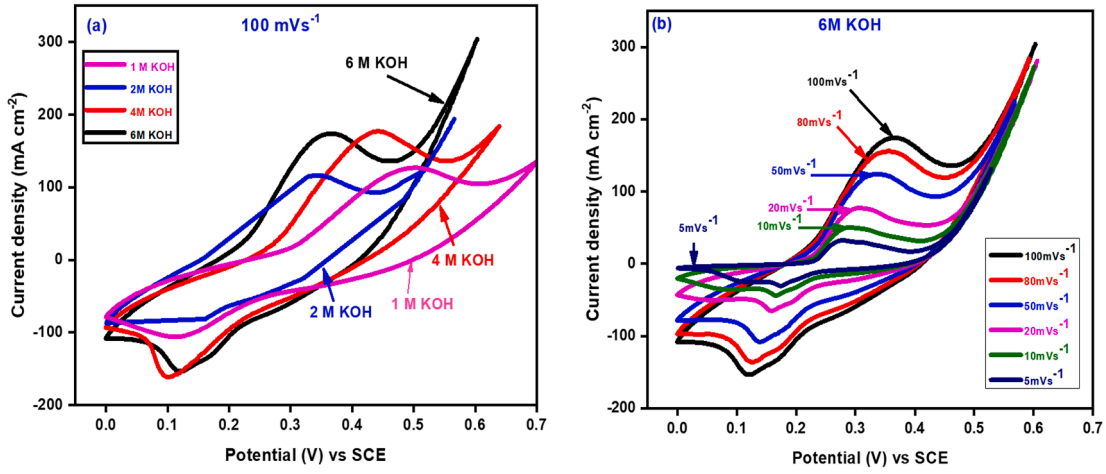

Fig. 4B. (a) Comparative CV plots of the NMO1 electrode in 1 M, 2 M, 4 M and 6 M KOH electrolyte at a scan rate of 100 mV s^{-1} (b) CV plots of the NMO1 electrode in 6 M KOH electrolyte obtained by varying scan rates.

Table 2
Summarized data of the calculated specific capacitance of the NMO1 electrode using CV plots and GCD plots in aqueous 1 M KOH and 6 M KOH electrolyte.

Method used to determine specific capacitance of NMO1 electrode	Measuring parameters	1 M KOH electrolyte						Measuring parameters	6 M KOH electrolyte					
CV	Scan rate (mVs^{-1})	5	10	20	50	80	100	Scan rate (mVs^{-1})	5	10	20	50	80	100
	Specific capacitance (Fg^{-1})	571	330	205	114	93	80	Specific capacitance (Fg^{-1})	762	440	274	152	125	107
GCD	Current density ($mAcm^{-2}$)	1	2	3				Current density ($mAcm^{-2}$)	1	2	3			
	Specific capacitance (Fg^{-1})	503	313	300				Specific capacitance (Fg^{-1})	612	381	365			

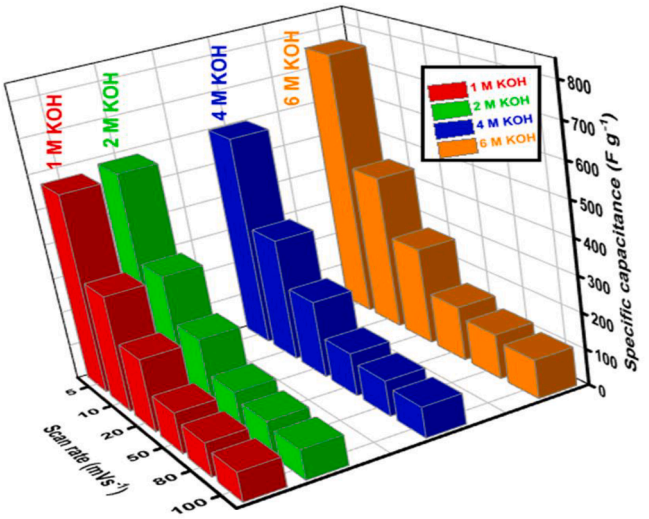

Fig. 4C. Plot of specific capacitance the NMO1 electrode vs. scan rate, in 1 M, 2 M, 4 M, and 6 M KOH electrolyte.

due to M−O−H bond [28]. Therefore, the formation of a pure phase spinel NMO is confirmed from the XPS analysis, which is in good agreement with XRD and FT-IR study.

3.3. Morphological study

Fig. 3A shows the FE-SEM micrographs of (a) NMO1 (b) NMO2 (c) NMO3, respectively. The surface morphology reveals the agglomerated coalescence nature of the NMO nanoparticles, which can be ascribed to interfacial surface tension. With an increase in the calcination temperature from 500 °C to 700 °C, particle size has also increased as shown in Fig. 3A (a-c).

3.4. BET analysis of the NMO1 powder

BET analysis is performed to examine the specific surface area of the NMO1 powder. Nitrogen adsorption–desorption isotherms of the NMO1 are displayed in Fig. 3B. The parallel Barrett-Joyner-Halenda (BJH) pore size distribution curve of the NMO1 is shown in the inset of Fig. 3B. It is found that the NMO1 has a large surface area of 39.32 m^2g^{-1} and the average pore diameter is determined as 26 nm in the mesoporous region of the NMO1.

3.5. Electrochemical properties

3.5.1. CV study

Organic electrolytes such as acetonitrile are flammable, extremely toxic, less conducting, and costly. In the present work instead of organic electrolytes, an aqueous KOH electrolyte is used because of its high electrical conductivity and low price. It provides a suitable assembly in the air due to its non-flammable nature.

The specific capacitance is directly proportional to the area under the CV plot. As shown in Fig. 4A (a), the area under the CV plot of bare Ni-foam is almost negligible as compared to the NMO1-Ni-foam. It confirms that the influence of bare Ni-foam in total capacitance is almost negligible and is consistent with the reported literature [20]. Due to the redox voltage of Ni^{2+}/Ni^{3+} and Mn^{2+}/Mn^{3+} the pair of redox peaks is found in the CV plot at 0.35 V for oxidation and 0.21 V for reduction, respectively, at a low scan rate of 5 mVs^{-1}. This signifies the pseudo capacitive behavior of the NMO1electrode. Faradic reactions depend on the intercalation–deintercalation of the electrolyte ions and are connected with the origination of redox peaks. In the present case, the Faradic reactions are represented by the following Eqs. (4) and (5).

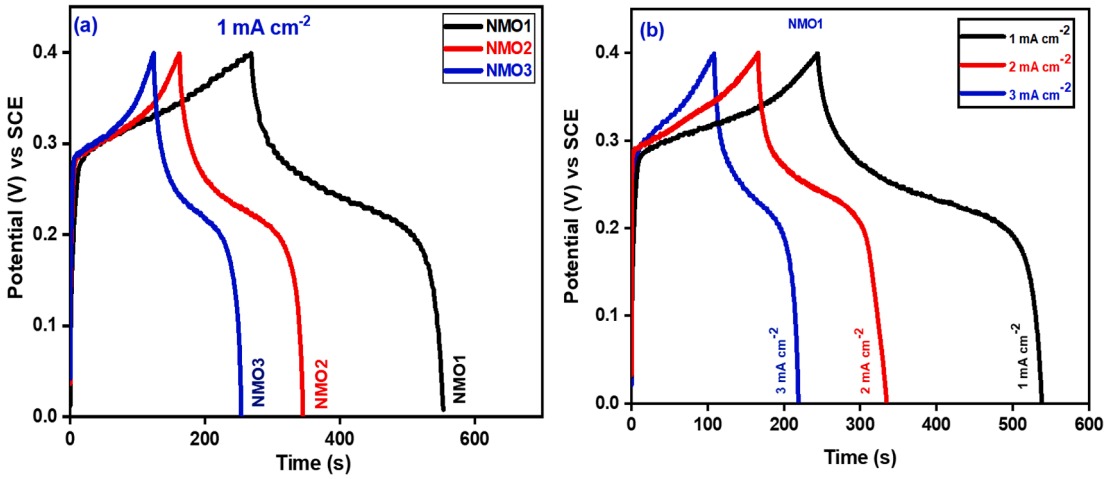

Fig. 5A. (a) Comparative GCD plots of the NMO1, NMO2 and NMO3 electrodes at a current density of 1 $mAcm^{-2}$ in 1 M KOH electrolyte. (b) GCD plots of the NMO1 electrode in 1 M KOH electrolyte obtained by varying current densities.

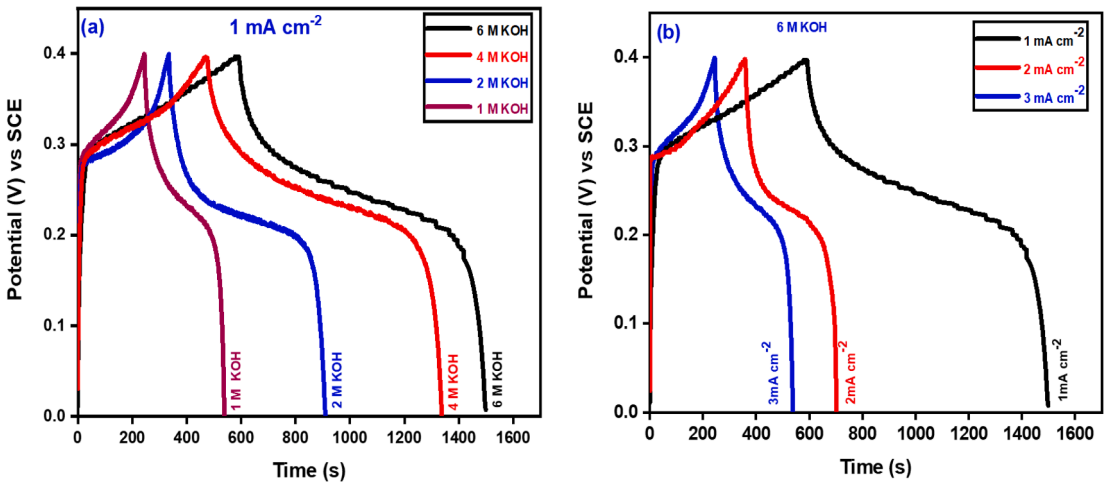

Fig. 5B. (a) Comparative GCD plots of the NMO1 electrode in 1 M, 2 M, 4 M, and 6 M KOH electrolyte at a current density of 1 $mAcm^{-2}$. (b) GCD plots of the NMO1 electrode in 6 M KOH electrolyte obtained by varying current densities.

$$NiMn_2O_4 + OH^- + H_2O \leftrightarrow NiOOH + 2MnOOH + 2e^- \quad (4)$$

$$MnOOH + OH^- \leftrightarrow MnO_2 + H_2O + e^- \quad (5)$$

The specific capacitance of the NMO1, NMO2, and NMO3 electrodes is calculated from the CV plots using the following Eq. (6).

$$C_{sp} = \frac{1}{2 \times (V_f - V_i) \times m} \int_{V_i}^{V_f} I(V)dv \quad (6)$$

where C_{sp} is the specific capacitance of NMO electrodes (Fg^{-1}), V is the scan rate (mVs^{-1}), m is the mass of the NMO electrode material (g), (V_f -V_i) is the applied potential window, and the integral term represents the area under the CV plot.

At a scan rate of 5 mVs^{-1}, the specific capacitance of the NMO1, NMO2, and NMO3 electrodes in 1 M KOH electrolyte is determined as 571 Fg^{-1}, 475 Fg^{-1}, and 337 Fg^{-1}, respectively. The specific capacitance of the NMO1 electrode is found to be better than NMO2 and NMO3. The surface morphology of the working electrode material implemented for supercapacitor application strongly influences its performance. The inferior performance of the NMO3 electrode over NMO1 and NMO2 can be attributed to its larger particle size, which reduces the active surface area and deteriorates the intercalation–deintercalation rates of the ions across the electrode–electrolyte boundary [29].

Fig. 4A(b) shows the comparative CV plots of the NMO1, NMO2, and NMO3 electrodes in 1 M KOH electrolyte at a scan rate of 100 mVs^{-1}, from which it is revealed that the NMO1 has a large expanse of the CV curve than NMO2 and NMO3 electrodes. CV plots of the NMO1 electrode in a cell containing 1 M KOH electrolyte at different scan rates are displayed in Fig. 4A(c). The specific capacitance of the NMO1 electrode at different scan rates in 1 M KOH electrolyte is determined by Eq. (6) and the improvement in the specific capacitance is observed with lowering of the scan rates. At a low scan rate, OH^- ions get sufficient time for the intercalation and improve the utilization rate of the working electrode [24]. Therefore, the specific capacitance of the NMO1 electrode increases with a decrease in the scan rates.

Fig. 4B (a) shows the comparative CV plots of the NMO1 electrode in a cell containing 1 M, 2 M, 4 M, and 6 M KOH electrolyte at a scan rate of 100 mVs^{-1}. It is seen that area of the CV curve of the NMO1 electrode in a cell containing 6 M KOH is larger than that of 1 M, 2 M, and 4 M KOH electrolyte. With an increase in the concentration of KOH electrolyte from 1 M to 6 M, the specific capacitance of the NMO1 electrode increases from 571 Fg^{-1} to 762 Fg^{-1}. Fig. 4B (b) shows the CV plots of the NMO1 electrode in a cell containing 6 M KOH electrolyte at various scan rates. Table 2 summarizes the specific capacitance values of the NMO1 electrode determined from the CV plots at different scan rates in 1 M and 6 M KOH electrolyte.

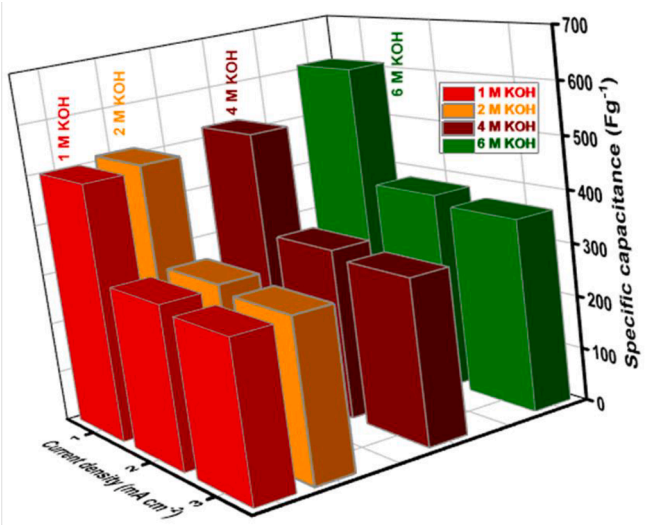

Fig. 5C. Plot of specific capacitance of the NMO1 electrode vs. current density, in 1 M, 2 M, 4 M and 6 M KOH electrolyte.

Fig. 4C displays the plot of the specific capacitance of the NMO1 electrode vs. scan rate, in a cell containing 1 M, 2 M, 4 M, and 6 M KOH electrolyte, from which it is perceived that at lower scan rates the NMO1 electrode exhibit notable specific capacitance with the varying concentration of KOH electrolyte from 1 M to 6 M.

3.5.2. GCD and EIS study

Fig. 5A(a) shows the comparative GCD plots of the NMO1, NMO2, and NMO3 electrodes in 1 M KOH electrolyte at a current density of 1 $mAcm^{-2}$. Nonlinear patterns of the GCD curves are resulting from the Faradic reactions occurring at the electrode–electrolyte interface and represent the pseudocapacitive nature of the electrode material. The specific capacitance of the NMO1, NMO2, and NMO3 electrodes from the GCD plots is evaluated by Eq. (7).

$$C_{sp} = \frac{I_{dis} \times \Delta t}{(V_f - V_i) \times m} \quad (7)$$

where C_{sp} is the specific capacitance, Δt is the discharge time, I_{dis} is the discharge current, m is the mass of the NMO electrode material,

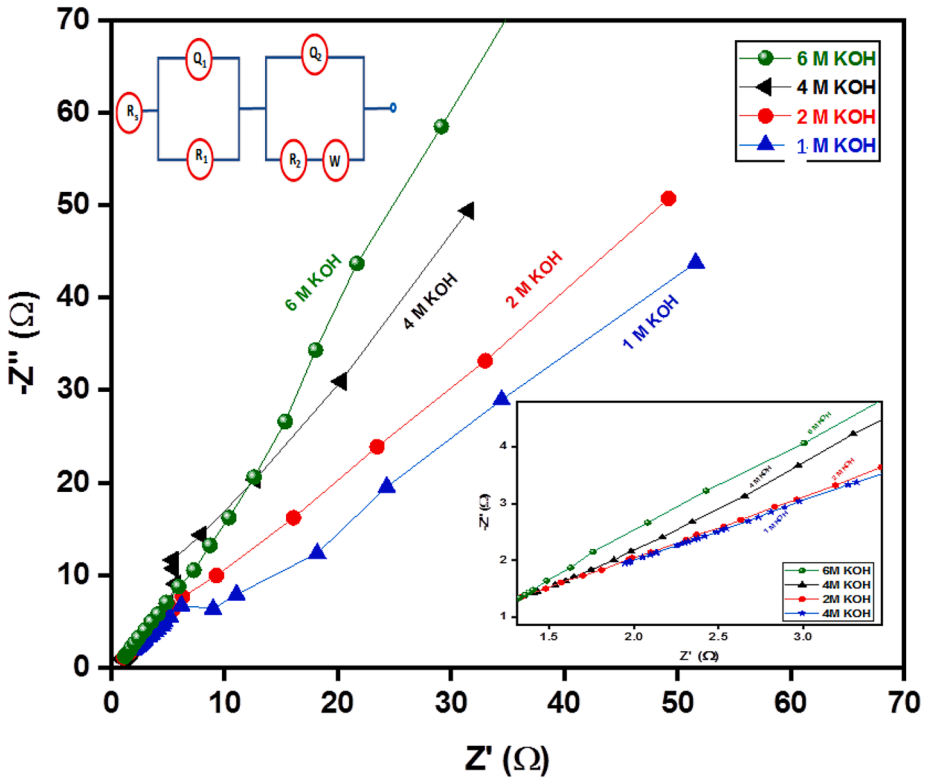

Fig. 6. Nyquist plot of the NMO1 electrode in 1 M, 2 M, 4 M, and 6 M KOH electrolyte.

Table 3
EIS parameters for NMO1-NF electrode in 1 M, 2 M, 3 M and 6 M KOH electrolyte.

Electrolyte	$R_s(\Omega)$	$R_{ct}(\Omega)$	Q_1 (mF)	Q_2 (mF)	W
1 M KOH	0.7	8.2	1.4	1.1	0.018
2 M KOH	0.51	4.46	1.9	1.3	0.061
4 M KOH	0.47	3.9	2.7	1.5	0.083
6 M KOH	0.32	3.33	3.2	1.9	0.094

and$(V_f - V_i)$ is the potential window. At a current density of 1 $mAcm^{-2}$, the specific capacitance of the NMO1, NMO2, and NMO3 electrodes in 1 M KOH electrolyte is determined as 503 Fg^{-1}, 474 Fg^{-1}, and 337 Fg^{-1}, respectively.

Fig. 5A (b) shows the GCD plots of the NMO1 electrode in 1 M KOH electrolyte with varying current densities. The specific capacitance of the NMO1 electrode is calculated by Eq. (7) from the GCD plots. It is found that the specific capacitance of the NMO1 electrode decreases with an increase in current density. This can be ascribed to ruining the utilization rate of the working electrode at higher current density, due to lowering of the intercalation rates of charged ions at the electrode–electrolyte interface.

Fig. 5B (a) represents the comparative GCD plots of the NMO1 electrode in 1 M, 2 M, 4 M, and 6 M KOH electrolyte at a current density of 1 $mAcm^{-2}$. The NMO1 electrode exhibits maximum specific capacitance of 612 Fg^{-1} in a cell containing 6 M KOH electrolyte. Fig. 5B (b) shows the GCD plots of the NMO1 electrode in a cell containing 6 M KOH electrolyte at different current densities. The specific capacitance values of the NMO1 electrode determined from the GCD plots at the various current densities in 1 M and 6 M KOH electrolytes are listed in Table 2.

Fig. 5C shows the plot of the specific capacitance of the NMO1 electrode vs. current density in a cell containing 1 M, 2 M, 4 M, and 6 M KOH electrolyte, which intends that at a lower current density the NMO1 electrode exhibit appreciable specific capacitance with the varying concentration of KOH electrolyte from 1 M to 6 M.

The electrochemical parameters such as specific energy (E_{sp}, $Whkg^{-1}$), specific power (P_{sp}, Wkg^{-1}), and Coulombic efficiency (η, %) of the NMO1 electrode in 6 M KOH electrolyte are calculated by Eqs. (8), (9), and (10) respectively [30].

$$E_{sp} = \frac{0.5 \times C_{sp} \times V^2}{3.6} \tag{8}$$

$$P_{sp} = \frac{3600 \times E_{sp}}{T_d} \tag{9}$$

$$\eta = \frac{T_d}{T_c} \times 100 \tag{10}$$

where C_{sp} is the specific capacitance determined from Eq. (7), V is the range of potential window, andT_c is the charge time, and T_d is the discharge time.

The value of specific energy, specific power, and Coulombic efficiency of the NMO1 electrode in 6 M KOH electrolyte is determined as 11.9 $Whkg^{-1}$, 44.4 Wkg^{-1}, and 98.2 %, respectively, at a current density of 1 $mAcm^{-2}$. Therefore, it can be inferred that the NMO1 electrode has a significant energy storage capacity and reflects good charge–discharge performance.

The frequency response and internal resistance of the cell containing NMO1 electrode with the varying concentration of KOH electrolyte has been determined by EIS. Fig. 6 shows the comparative EIS plots of the NMO1 electrode in a cell containing 1 M, 2 M, 4 M, and 6 M KOH electrolyte. The inset of the Fig. 6 shows equivalent circuit used for fitting the Nyquist plot. The internal resistance (R_s) of the cell consists of intrinsic resistance of the electrode material, contact resistance between current collector and electrode, and resistance offered by an electrolyte. R_{ct} is the charge transfer resistance resulting from the Faradic reactions at the electrode–electrolyte boundary [31]. EIS analysis has provided the values of R_s and R_{ct} as 0.7 Ω, and 8.2 Ω, in 1 M KOH, 0.51 Ω, and 4.46 Ω, in 2 M KOH, 0.47 Ω, and 3.9 Ω, in 4 M KOH, 0.32 Ω, and 3.33 Ω, in 6 M KOH electrolyte, respectively. For the NMO1 electrode, the values

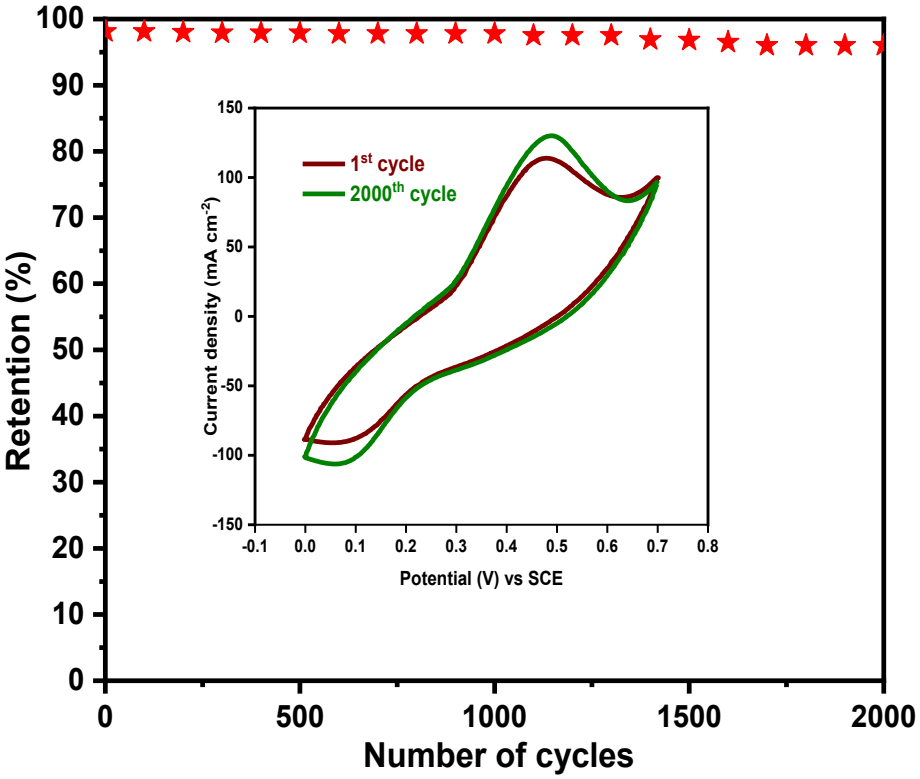

Fig. 7. Plot of capacitance retention rate of the NMO1 electrode vs. cycle number in 6 M KOH electrolyte.

Table 4
Comparison of specific capacitance of the NMO based electrode material from the present research work with other research groups in accordance with, the synthesis method used for preparation of NMO, the electrolyte used, current collector utilized, and % retention of specific capacitance after number of cycles.

Method of preparation	Electrolyte	Current collector	Specific capacitance (Fg^{-1})	Retention %/ cycles	Reference
Sol - gel	1 M Na_2SO_4	Ni-mesh	243	96/5000	[11]
Spray pyrolysis	2 M KOH	FTO	460	92.97/1000	[12]
Hydrothermal	6 M KOH	Ni- foil	368	–	[26]
Sol - gel	1 M KOH	Ni-foam	303	–	[34]
Hydroxide precipitation.	1 M $LiNO_3$	Stainless steel wire mesh.	184	–	[35]
Calcination	1 M Na_2SO_4	Ni-grid	180	92.8/1000	[36]
Hydrothermal	2 M KOH	Ni-foam	236.9	–	[37]
Electro spinning process	1 M KCl	Graphite sheet	410 (±5)	95/5000	[38]
Sol - gel	6 M KOH	Ni - foam	762	96/2000	This work

of R_s and R_{ct} determined in 6 M KOH are lower than the values obtained at other concentrations of KOH electrolyte. The value of R_s and R_{ct} is the determining factor of the specific power given by supercapacitor [32]. Therefore, the superior performance of the NMO1 electrode observed in 6 M KOH over the other concentrations of KOH electrolyte can be ascribed to smaller values of R_s and R_{ct}. The EIS parameters for NMO1 electrode in 1 M, 2 M, 4 M, and 6 M KOH electrolyte have been calculated and summarized in Table 3.

3.5.3. *Cyclic stability study*

Long-term cyclic stability of the working electrode is very essential for the supercapacitor application [33]. The cyclic performance of the NMO1 electrode is tested in a cell containing 6 M KOH electrolyte by employing the CV technique. Fig. 7 displays the plot of capacitance retention rate of the NMO1 electrode vs. cycle number for 2000 cycles. The NMO1 electrode retained 96 % of the capacitance after 2000 cycles in 6 M KOH electrolyte.

The comparison of the specific capacitance obtained, current collector utilized, the electrolyte used, synthesis approach involved and capacitance retention after the number of cycles of NMO based electrode material from the present research work with other research groups is represented in Table 4.

4. Conclusions

The XRD analysis confirmed that sol–gel-derived NMO powders exhibit cubic structure with the F-space group. With an increase in calcination temperature from 500 °C to 700 °C, the average crystallite size of the NMO powders has increased from 9.7 nm to 19 nm. FE-SEM micrographs reflected the porous nature of the NMO1 powder. BET analysis revealed the average pore diameter and surface area of the NMO1 powder as of 26 nm, and 39.32 m^2g^{-1}, respectively. At a scan rate of 5 $mVs^{-1}$the specific capacitance of the NMO1electrode is improved from 571 Fg^{-1} to 762 Fg^{-1}, with an increase in the concentration of KOH electrolyte from 1 M to 6 M. The maximum specific capacitance of the NMO1 electrode in a cell containing 6 M KOH electrolyte can be ascribed to the large expanse of the CV curve and smaller values of R_s and R_{ct}. The NMO1 electrode exhibit 96 % cyclic stability for 2000 cycles with specific energy and specific power of 11.9 $Whkg^{-1}$ and 44.4 $kWkg^{-1}$, respectively in 6 M KOH electrolyte.

The present results suggest that NMO electrode materials are prominent candidates for the fabrication of electrochemical capacitors.

The charge exchange rate across the electrode–electrolyte interface is determined by the particle size of the electrode material and the concentration of the electrolyte. Therefore, electrode material with suitable porosity and electrolyte with appropriate concentration will be beneficial for fabricating efficient electrochemical capacitors.

Declaration of Competing Interest

The authors declare that they have no known competing financial interests or personal relationships that could have appeared to influence the work reported in this paper.

Acknowledgments

Author S.D. Dhas acknowledges Chhatrapati Shahu Maharaj Research, Training and Human Development Institute (SARTHI), Pune and DST-SERB [SERB/F/1699/2018-19] for providing funding. All the authors also wish to acknowledge the Special Assistance Program (SAP) [F.530/16/DSA-II/2018 (SAP-II)] and PIFC (Physics Instrumentation Facility Centre), Department of Physics Shivaji University, Kolhapur, for providing characterization facilities for the present research work.

References

[1] S. Balasubramaniam, A. Mohanty, S.K. Balasingam, S.J. Kim, A. Ramadoss, Comprehensive insight into the mechanism, material selection and performance evaluation of supercapatteries vol. 175, Springer, Singapore, 2020, pp. 534–575, 10.1007/s40820-020-0413-7.

[2] P. Simon, Y. Gogotsi, Materials for electrochemical capacitors, Nat. Mater. 7 (11) (2008) 845–854, https://doi.org/10.1038/nmat2297.

[3] S.D. Dhas, P.S. Maldar, M.D. Patil, K.M. Hubali, U.V. Shembade, S.B. Abitkar, M. R. Waikar, R.G. Sonkawade, G.L. Agawane, A.V. Moholkar, Hydrothermal synthesis of mesoporous $NiMnO_3$ nanostructures for supercapacitor application: Effect of electrolyte, J. Energy Storage 35 (2021) 102277, https://doi.org/10.1016/j.est.2021.102277.

[4] J. Miller, P. Simon, Electrochemical capacitors for energy management, Sci. Mag. 321 (2008) 651–652, https://doi.org/10.1126/science.1158736.

[5] C. Zhong, Y. Deng, W. Hu, J. Qiao, L. Zhang, J. Zhang, A review of electrolyte materials and compositions for electrochemical supercapacitors, Chem. Soc. Rev. 44 (2015) 7484–7539, https://doi.org/10.1039/c5cs00303b.

[6] M. Hadj-Sadok, A. Benadda, A. Kiennemann, A. Barama, Preparation and catalytic activity of nickel manganese oxide catalysts in the reaction of partial oxidation of methane, C R. Chimie 12 (6–7) (2009) 740–747, https://doi.org/10.1016/j.crci.2008.12.002.

[7] K. Vijaya Sankar, S. Surendran, K. Pandi, A.M. Allin, V.D. Nithya, R. Kalai Selvan, Studies on the electrochemical intercalation/de-intercalation mechanism of NiMn2O4 for high stable pseudocapacitor electrodes, RSC Adv. 5 (2015) 27649, https://doi.org/10.1039/c5ra00407a.

[8] T. Larbi, L. Ben said, A. Ben daly, B. ouni, A. Labidi, M. Amlouk, Ethanol sensing properties and photocatalytic degradation of methylene blue by Mn_3O_4, $NiMn_2O_4$ and alloys of Ni- manganates thin films, J. Alloys Compd. 686 (2016) 168–175, https://doi.org/10.1016/j.jallcom.2016.06.001.

[9] H. Gao, C. Ma, B. Sun, Preparation and characterization of $NiMn_2O_4$ negative temperature coefficient ceramics by solid-state coordination reaction, J Mater Sci: Mater Electron 25 (9) (2014) 3990–3995, https://doi.org/10.1007/s10854-014-2118-5.

[10] J.A. Almeida, C.T. Meneses, A.S. de Menezes, R.F. Jardim, J.M. Sasaki, Synthesis and characterization of $NiMn_2O_4$ nanoparticles using gelatin as organic precursor, J. Magn. Magn. Mater. 320 (14) (2008) 304–307, https://doi.org/10.1016/j.jmmm.2008.02.062.

[11] M. Zhang, S. Guo, L. Zheng, G. Zhang, Z. Hao, L. Kang, Z. Liu, Preparation of $NiMn_2O_4$ with large specific surface area from an epoxide-driven sol-gel process and its capacitance, Electrochim. Acta 87 (2013) 546–553, https://doi.org/10.1016/j.electacta.2012.09.085.

[12] U.J. Chavan, A.A. Yadav, Electrochemical behavior of spray deposited mixed nickel manganese oxide thin films for supercapacitor applications, J Mater Sci: Mater Electron. 28 (6) (2017) 4958–4964, https://doi.org/10.1007/s10854-016-6148-z.

[13] J. Topfer, A. Feltz, D. Gräf, B. Hackl, L. Raupach, P. Weissbrodt, Cation valencies and distribution in the spinels $NiMn_2O_4$, and MzNiMn2-zO4(M = Li, Cu) Studied by XPS, Phys. Stat. 134 (1992) 405–415, https://doi.org/10.1002/pssa.2211340211.

[14] Y. Gawli, S. Badadhe, A. Basu, D. Guin, M. Shelke, S. Ogale, Evaluation of n-type ternary metal oxide $NiMn_2O_4$ nanomaterial for humidity sensing, Sens. Act. B 191 (2014) 837–843, https://doi.org/10.1016/j.snb.2013.10.071.

[15] M. Tadic, S. Savic, Z. Jaglicic, K. Vojisavljevic, A. Radojkovic, S. Prsic, D. Nikolic, Magnetic properties of $NiMn_2O_{4-\delta}$ (nickel manganite): Multiple magnetic phase transitions and exchange bias effect, J. Alloys Compd. 588 (2014) 465–469, https://doi.org/10.1016/j.jallcom.2013.11.025.

[16] G. Ashcroft, I. Terry, R. Gover, Study of the preparation conditions for $NiMn_2O_4$ grown from hydroxide precursors, J. Eur. Ceram 26 (6) (2006) 901–908, https://doi.org/10.1016/j.jeurceramsoc.2004.11.023.

[17] C. Lin, D. Shi, Z. Wu, L. Zhang, Z. Zhai, Y. Fang, P. Sun, R. Han, J. Wu, H. Liu, $CoMn_2O_4$ catalyst prepared using the sol-gel method for the activation of peroxymonosulfate and degradation of UV filter 2- Phenylbenzimidazole- 5-sulfonic Acid (PBSA), Nanomaterials 9 (2019) 774, https://doi.org/10.3390/nano9050774.

[18] J.F. Marco, J.R. Gancedo, M. Gracia, J.L. Gautier, E. Rios, F.J. Berry, Characterization of the nickel cobaltite, $NiCo_2O_4$, prepared by several methods: an XRD, XANES, EXAFS, and XPS study, J. Solid State Chem. 153 (2000) 74–81, https://doi.org/10.1006/jssc.2000.8749.

[19] P. Sen, A. De, Electrochemical performances of poly (3, 4-ethylenedioxythiophene)-$NiFe_2O_4$ nanocomposite as electrode for supercapacitor, Electrochim. Acta. 55 (16) (2010) 4677–4684, https://doi.org/10.1016/j.electacta.2010.03.077.

[20] A. Ray, A. Roy, M. Ghosh, J.A. Ramos-ramón, S. Saha, U. Pal, S. Bhattacharya, S. Das, Study on charge storage mechanism in working electrodes fabricated by sol-gel derived spinel $NiMn_2O_4$ nanoparticles for supercapacitor application, Appl. Surf. Sci. 463 (2019) 513–525, https://doi.org/10.1016/j.apsusc.2018.08.259.

[21] S. Vijayakumar, S. Nagamuthu, G. Muralidharan, Supercapacitor studies on NiO nano flakes synthesized through a microwave route, ACS Appl. Mater. Interfaces 5 (2013) 2188–2196, https://doi.org/10.1021/am400012h.

[22] S.A. Hosseini, A. Niaei, D. Salari, S.R. Nabavi, Nanocrystalline AMn_2O_4 (A = Co, Ni, Cu) spinels for remediation of volatile organic compounds-synthesis, characterization and catalytic performance, Ceram. Int 38 (2) (2012) 1655–1661, https://doi.org/10.1016/j.ceramint.2011.09.057.

[23] D.R. Baer, M.H. Engelhard, XPS analysis of nanostructured materials and biological surfaces, J. Electron Spectrosc. Relat. Phenom. 178–179 (2010) 415–432, https://doi.org/10.1016/j.elspec.2009.09.003.

[24] S. Wang, J. Pu, Y. Tong, Y. Cheng, Y. Gao, Z. Wang, $ZnCo_2O_4$ nanowire arrays grown on nickel foam for high-performance pseudocapacitors, J. Mater. Chem. A, 2 (2014) 5434–5440, https://doi.org/10.1039/C3TA14941B.

[25] L. Li, H. Hu, S. Ding, Facile synthesis of ultrathin and perpendicular $NiMn_2O_4$nanosheets on reduced graphene oxide as advanced electrodes for supercapacitors Inorg, Chem. Front. 5 (2018) 1714–1720, https://doi.org/10.1039/C8QI00121A.

[26] H. Nan, W. Ma, Z. Gu, B. Geng, X. Zhang, Hierarchical $NiMn_2O_4$@CNT Nanocomposites for High-Performance Asymmetric supercapacitors, RSC Adv. 5 (31) (2015) 24607–24614, https://doi.org/10.1039/C5RA00979K.

[27] S. Sahoo, S. Zhang, J. Shim, Porous ternary high performance supercapacitor electrode based on reduced graphene oxide, $NiMn_2O_4$, and polyaniline, Electrochim. Acta 216 (2016) 386–396, https://doi.org/10.1016/j.electacta.2016.09.030.

[28] N. Duraisamy, A. Numan, S. Fatin, K. Ramesh, S. Ramesh, Facile sonochemical synthesis of nanostructured NiO with different particle sizes and its electrochemical properties for supercapacitor application, J. Colloid Interface Sci. 471 (2016) 136–144, https://doi.org/10.1016/j.jcis.2016.03.013.

[29] S. Pilban Jahromi, A. Pandikumar, B.T. Goh, Y.S. Lim, W.J. Basirun, H.N. Lim, N. M. Huang, Influence of particle size on performance of a nickel oxide nanoparticle-based supercapacitor, RSC Adv. 5 (18) (2015) 14010–14019, https://doi.org/10.1039/C4RA16776G.

[30] R.R. Salunkhe, M.B. Zakaria, Y. Kamachi, S.M. Alshehri, T. Ahamad, N.L. Torad, S. X. Dou, J.H. Kim, Y. Yamauchi, Fabrication of asymmetric supercapacitors based on coordination polymer derived nanoporous materials, Electrochim. Acta 183 (2015) 94–99, https://doi.org/10.1016/j.electacta.2015.05.034.

[31] P. Gao, P. Metz, T. Hey, Y. Gong, D. Liu, D.D. Edwards, J.Y. Howe, R. Huang, S. T. Misture, The critical role of point defects in improving the specific capacitance of δ-MnO_2 nanosheets, Nat. Commun. 8 (2017), https://doi.org/10.1038/ncomms14559.

[32] R.B. Rakhi, W. Chen, D. Cha, H.N. Alshareef, High performance supercapacitors using metal oxide anchored graphene nanosheet electrodes, J. Mater. Chem. 21 (40) (2011) 16197, https://doi.org/10.1039/c1jm12963e.

[33] D. Li, Y. Gong, Y. Zhang, C. Luo, W. Li, Q. Fu, C. Pan, Facile synthesis of carbon nanosphere/$NiCo_2O_4$ core shell sub-microspheres for high performance supercapacitor, Sci. Rep. 5 (2015) 12903, https://doi.org/10.1038/srep12903.

[34] B.N. Vamsi Krishna, J. Bhagwan, J.S. Yu, sol-gel routed $NiMn_2O_4$ nanofabric electrode materials for supercapacitors, J. Electrochem. Soc. 166 (2019) A1950–A1955, https://doi.org/10.1149/2.0661910jes.

[35] M.Y. Arsent'ev, N.Y. Koval'ko, A.V. Shmigel', P.A. Tikhonov, M.V. Kalinina, $NiMn_2O_4$ spinel as a material for supercapacitors with a pseudocapacity effect, Glass Phys. Chem. 43 (2017) 376–379, https://doi.org/10.1134/S1087659617040022.

[36] H. Pang, J. Deng, S. Wang, S. Li, J. Du, J. Chena, J. Zhang, Facile synthesis of porous nickel manganite materials and their morphology effect on electrochemical properties, RSC Adv. 2 (2012) 5930–5934, https://doi.org/10.1039/c2ra20245j.

[37] M.R. Kim, R.M. NaiduKalla, S. Kim, M.R. Kim, I. Kim, $NiMn_2O_4$ nano-sheet decorated hierarchically porous polyaromatic carbon spheres for high-performance supercapacitors, Chem. Electro. Chem. 4 (2017) 1214–1221, https://doi.org/10.1002/celc.201700023.

[38] J. Bhagwan, S. Rani, V. Sivasankaran, K. Yadav, Y. Sharma, Improved energy storage, magnetic and electrical properties of aligned, mesoporous and high aspect ratio nanofibers of spinel-$NiMn_2O_4$, Appl. Surf. Sci. 426 (2017) 913–923, https://doi.org/10.1016/j.apsusc.2017.07.253.